

Proximity SQUID Single-Photon Detector via Temperature-to-Voltage Conversion

P. Solinas,^{1,*} F. Giazotto,² and G. P. Pepe^{3,1}

¹SPIN-CNR, Via Dodecaneso 33, 16146 Genova, Italy

²NEST, Istituto Nanoscienze-CNR and Scuola Normale Superiore, I-56127 Pisa, Italy

³Università di Napoli Federico II, Monte Sant'Angelo, I-80125 Napoli, Italy



(Received 29 November 2017; revised manuscript received 17 March 2018; published 13 August 2018)

We propose a single-photon detector based on a superconducting quantum interference device (SQUID) with superconductor–normal-metal–superconductor Josephson weak links. One of the two Josephson junctions is connected to an antenna, and is heated when a photon is absorbed. The increase of the weak-link temperature exponentially suppresses the Josephson critical current, thereby inducing an asymmetry in the SQUID. This generates a voltage pulse across the SQUID that can be measured with a threshold detector. Realized with realistic parameters, the device can be used as a single-photon detector—and as a calorimeter, since it is able to discriminate photon frequencies above 5 THz with a signal-to-noise ratio larger than 20. The performance of the detector is robust with respect to working temperatures between 0.1 and 0.5 K, and with respect to thermal noise perturbation.

DOI: 10.1103/PhysRevApplied.10.024015

I. INTRODUCTION

Photon-counting detectors demonstrating the highest sensitivity and efficiency have become indispensable for many applications in the visible and near-infrared electromagnetic range, such as space-to-ground communications [1] or quantum key distribution [2]. The benchmark for a solid-state single-photon detector is determined by the avalanche photodiodes, but in 2001 a novel superconducting single-photon optical detector was proposed [3]. The main advantages of this device are its sensitivity at visible and infrared wavelengths, and its ability to work at relatively high temperature, i.e., 4.2 K, and to be more sensitive than the Si avalanche photodiode in the long-wavelength region [4]. In the past decade, there has been increased interest followed by considerable technological development [4]. This includes an improvement in coupling efficiency, using a nanowire meander [5], in absorption efficiency, using a nanowire in optical cavities [6,7], and in registering efficiency, using an ultranarrow nanowire (of 20 or 30 nm) [8]. Fabrication with an alternative material to the original NbN has been proposed and tested [9–11]. The same devices are promising candidates for the detection of multiphoton events [12,13].

The additional need for high-sensitivity detectors in the THz region is of particular interest in many research fields, ranging from communications technology, through

astrophysics, to more exotic applications in quantum information. The far infrared, including the THz region, is a very important spectral range, since it contains about 98% of all the photons existing in the Universe: the availability of very efficient recording devices in the long-wavelength single-photon regime in this spectral range represents a truly exciting frontier in astronomy [14].

However, single-photon THz detectors are significantly limited by the difficulty in obtaining single-photon sensitivity due to the small amount of energy carried by an individual photon (i.e., typically 2–5 meV). This energy corresponds to a detector equivalent temperature of only a few tens of kelvins, and hence extremely low operating temperatures are needed to avoid thermal noise. Besides the first detection of single THz photons with semiconductor quantum dots (QDs), hot electrons, and superconducting bolometers [15–17], new and efficient detection schemes are needed. The possibility of using the physical properties of the superconducting state in Josephson-based devices represents an attractive degree of freedom to be explored due to their high charge and phase sensitivity in determining the final performance.

Here, we propose a design for a proximity superconducting quantum interference device (SQUID) radiation detector (PSRD) that can be used as a single-photon sensor and as a calorimeter, i.e., by measuring the frequency of the incident photon. A proximized normal metal in a long Josephson weak link (JWL) can be heated by absorption of the photon. The subsequent increase in its electronic temperature induces an instability in the interferometer that

*paolo.solinas@spin.cnr.it

generates a voltage pulse across the SQUID in order to relax to a stable state. The key point in the process is the possibility of setting the SQUID close to an instability point. In the present case, this can be done by adjusting the external magnetic flux piercing the interferometer.

This working principle is directly related to the observation that when we change the magnetic flux in a Josephson interferometer and cross such an instability point, the superconducting phase must undergo a phase jump [18,19]. This new physical phenomenon was originally discussed in Ref. [18] and indirectly observed in Ref. [20]. The extension to the full dynamical model has been carried out in Refs. [19,21,22]. In these later papers, the system was driven through an instability point by an external time-dependent magnetic flux. The control of the time-dependent magnetic field allows us to induce the phase jump and the corresponding voltage pulse at will. When subject to a periodic drive, the interferometer emits a voltage-pulse comb (a sequence of equally spaced and identical voltage pulses), as a complete analogy to the optical combs used in metrology [23].

The same idea is the basis for the present PSRD. We consider two JWLS in a superconducting quantum-interference device (SQUID) configuration [24]. By tuning the magnetic flux piercing the SQUID, we can set the device close to an instability point. When a photon is absorbed (through a suitable antenna coupled to one of the JWLS), it heats the JWL, inducing a phase jump and a voltage pulse. The detection of these voltage pulses gives us information about the arrival of the photon. When the detection electronics are able to distinguish additional information about the voltage pulse, e.g., its maximum, it is possible to discriminate the photon frequency and use the PSRD as a calorimeter.

From our analysis, a Nb-based PSRD can work well for photon frequencies above 5 THz. With a detector bandwidth of 10 GHz, the achievable signal-to-noise ratio and resolving power are large enough to discriminate both the arrival of the photon and its frequency. The PSRD can operate at sufficiently high temperature, i.e., a bath temperature of up to ~ 0.5 K, and it is robust against thermal noise.

II. A SINGLE JWL UNDER PHOTON ABSORPTION

First, we consider a single JWL consisting of a normal-metal (N) wire of length l coupled to two superconductors S via transparent contacts [25,26]. The JWL is coupled to an antenna that is able to collect the incident photon radiation at energy $h\nu$ [see Fig. 1(a)]. The latter heats the electrons in the normal-metal region, thereby increasing its electronic temperature T_e .

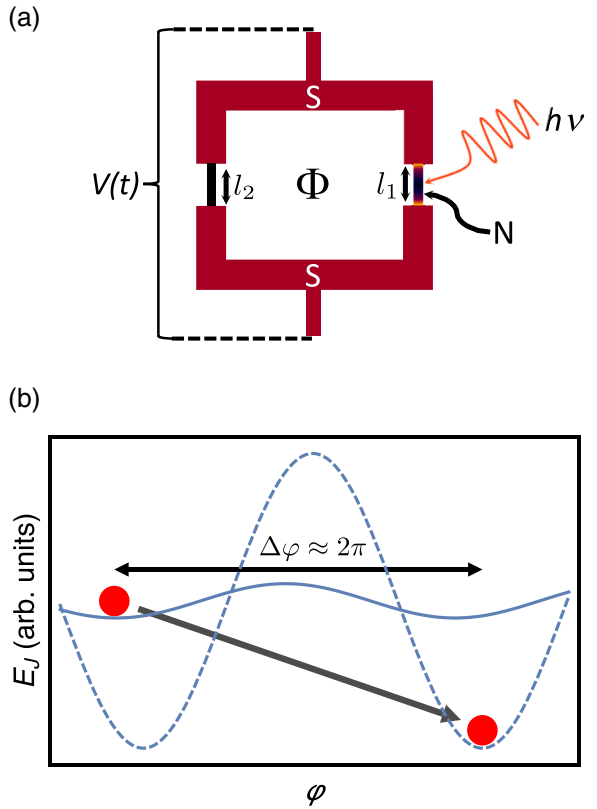


FIG. 1. (a) The scheme of the PSRD. Two SNS Josephson weak links are arranged in a SQUID configuration. One junction is connected to an antenna that absorbs the arriving photons at energy $h\nu$. The weak-link lengths are l_1 and l_2 , respectively, and the SQUID is pierced by an external magnetic flux Φ . The photon absorption generates a time-dependent voltage pulse $V(t)$ across the interferometer. (b) A pictorial representation of the induced instability. The Josephson energy E_J (in arbitrary units) is plotted before (solid blue curve) and after photon absorption (dashed blue curve). The change in the energy potential induces a dynamic in the phase particle (red circle) that jumps to a close minimum with a phase change $\Delta\varphi$ of about 2π .

We denote by Δ and D the gap of the superconductor S and the diffusion coefficient of the normal metal, respectively. If the Josephson junction is long, i.e., for $E_{\text{Th}} = \hbar D/l^2 \ll k_B T_e \ll \Delta$, where E_{Th} is the Thouless energy, the Josephson current of the junction is $I_J(T_e) = I_c(T_e) \sin \varphi$, where φ is the superconducting phase difference across the junction and, from Refs. [25,27,28],

$$I_c(T_e) = \frac{64\pi k_B T_e}{(3 + 2\sqrt{2}eR_N)} \sqrt{\frac{2\pi k_B T_e}{E_{\text{Th}}}} e^{-\sqrt{2\pi k_B T_e/E_{\text{Th}}}}. \quad (1)$$

Above, $R_N = \rho l / \mathcal{A}$ is the normal-state resistance of the wire (ρ and \mathcal{A} are the wire resistivity and cross section, respectively). In the following, we have used $D = 0.01 \text{ m}^2 \text{ s}^{-1}$ and $\rho = (v_F e^2 D)^{-1}$, with $v_F = 10^{47} \text{ J}^{-1} \text{ m}^3$ being the density of states at the Fermi level in the N

region [25]. The geometric parameters l and \mathcal{A} change from junction to junction and are chosen to maximize the performance of the device (see discussion below) but, as a reference, we can have (typical of silver, Ag) $L = 1 \mu\text{m}$ and $\mathcal{A} = 10^{-15} \text{ m}^2$, leading to $R_N = 38 \Omega$.

To determine the dynamics of the junction temperature, we follow Ref. [25]. We assume that a photon of frequency ν is absorbed at time t_0 in the volume Ω of the N region. We model the energy injection into the junction with a Gaussian pulse with standard deviation (in time) σ , so that the photon power is $P_\gamma = (2\pi\hbar\nu/\Omega\sqrt{2\pi}\sigma)e^{-(t-t_0)^2/(2\sigma^2)}$. The N region of the junction has an electronic thermal capacity $C_e = \pi^2\nu_F k_B^2 T_e/3$, and it is in contact with the phonon bath so that it can dissipate power (per unit of volume) as $P_{e\text{-ph}} = \Sigma(T_e^5 - T_{\text{bath}}^5)$, where Σ is the electron-phonon coupling constant in N [29]. The power-balance equation therefore reads as follows [25]:

$$C_e \frac{dT_e}{dt} = P_\gamma - P_{e\text{-ph}}. \quad (2)$$

In the following, we consider a volume of $\Omega = 10^{-21} \text{ m}^3$ and $\Sigma = 0.5 \times 10^9 \text{ W m}^3 \text{ K}^{-5}$, which are typical values for a silver junction.

An example of the behavior of $T_e(t)$ is shown in Fig. 2(a). The photon heats the junction up to a maximum of roughly $T_{e,\text{max}} = \sqrt{T_{\text{bath}}^2 + 12\hbar\nu/(\pi\Omega\nu_F k_B^2)}$, then the junction dissipates the energy excess over a timescale of the order of $\tau_{e\text{-ph}}$ [25]. Since, in general, the diffusion time along the N strip $\tau_D = l^2/D \approx \sigma \ll \tau_{e\text{-ph}}$ [25,29], where $\tau_{e\text{-ph}}$ is the electron-phonon interaction time ($\tau_{e\text{-ph}} \sim 10^{-4}\text{--}10^{-7} \text{ s}$ in the $0.1\text{--}1 \text{ K}$ temperature range), we can assume that the temperature of the junction remains almost constant after photon absorption, as shown in Fig. 2(a). If we define the relaxation time τ_R as the time needed for $T_e(\tau_R) = (T_{e,\text{max}} - T_{\text{bath}})/2$, with the parameter used for the numerics in Fig. 2, we obtain $\tau_R \approx 120 \text{ ns}$. This is much longer than $\tau_D \sim 0.1 \text{ ns}$ and σ (for the numerical simulation, we take $\sigma = 0.1 \text{ ns}$). In the present model, the relaxation time is the limiting factor for the photon detection rate. However, using different materials and different fabrication geometry, the energy dissipation to the phonon bath can be increased and, thus, the idle time can be reduced.

The mechanism responsible for the presence of a supercurrent in the superconductor–normal-metal–superconductor (SNS) junction is the *proximity* effect, which induces, in the N region, a local density of states with a minigap $E_g \approx 3.1E_{\text{Th}}$ [25,30]. In all of our analysis, we ignore the effect that such a modification induces in the heat capacity and the electron-phonon coupling [31–33]. Specifically, due to the presence of the minigap, both of these quantities are expected to be somewhat suppressed inside the N region, thereby improving the performance

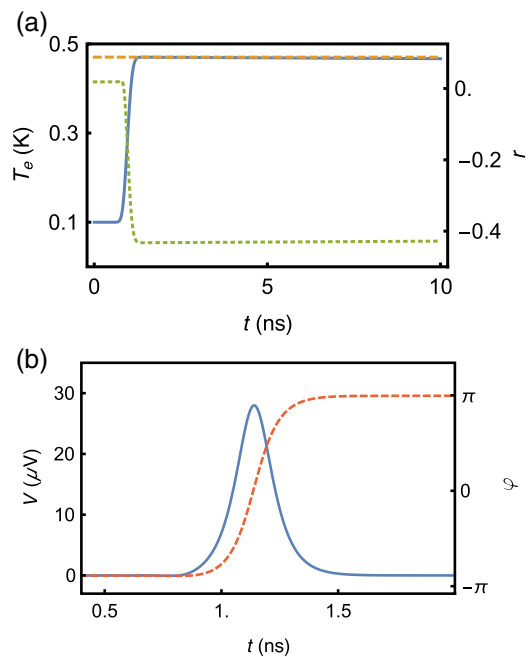


FIG. 2. (a) The temporal dynamics of the temperature T_e of the normal-metal region when a photon is absorbed (solid blue curve), and of the SQUID asymmetry parameter r (dotted green curve). The maximal temperature reached by the N region is shown as a dashed orange line. (b) The voltage (solid blue) and superconducting phase (dashed red) as a function of time due to photon absorption. The parameters used in the calculations are [25]: $T_{\text{bath}} = 0.1 \text{ K}$, $\Omega = 10^{-21} \text{ m}^3$, $\nu_F = 10^{47} \text{ J}^{-1} \text{ m}^3$ and $\Sigma = 0.5 \times 10^9 \text{ W m}^3 \text{ K}^{-5}$ [as appropriate for silver (Ag)], $D = 0.01 \text{ m}^2 \text{ s}^{-1}$, $l = 10^{-7} \text{ m}$, and $R_N = 38 \Omega$. The standard deviation of the Gaussian photon envelope is $\sigma = 0.1 \text{ ns}$.

of the PSRD. Moreover, a photon with energy ν can be absorbed in the junction if $\nu > 2E_{\text{Th}}/h$ [34,35]. For the typical junction parameters used in our calculations, we have $\nu > 3 \text{ GHz}$.

In the present analysis, we assume that when a photon is absorbed, all its energy is transferred to the junction generating the increase in temperature. This description is, of course, oversimplified. The absorption and the efficiency in the energy transfer depend on the details of the antenna, e.g., on the materials and the geometry. The antenna can be designed and optimized in order to work on a kind of photon property or a particular energy region. In the present paper, we do not deal with such details of the specific implementation; instead, we focus more on the physical mechanism underlying the photon detector.

III. THE DYNAMICS OF THE SQUID

To exploit the phase-jump effect discussed in Sec. I and Refs. [19,21,22], we consider two SNS Josephson weak links in a SQUID configuration. One of the JWLS, say junction 1, is coupled to an antenna and is heated by the photon, as shown in Fig. 1(a). The JWLS are supposed to

have the same resistance $R_{N,1} = R_{N,2} = R_N$ but different lengths, i.e., $l_1 \neq l_2$, in order to have different Thouless energies. Moreover, the junction length asymmetry is captured by the parameter $\epsilon = l_1/l_2$. Here, we assume that the ring inductance is negligible but a similar approach can be used in case of a non-vanishing ring inductance [36,37].

We denote by Φ the magnetic flux piercing the SQUID, and the current (I_J) vs phase relation of the SQUID reads [19]

$$I_J(\varphi; \phi) = I_+ [\cos \phi \sin \varphi + r \sin \phi \cos \varphi], \quad (3)$$

where φ_i is the phase across the i th junction, $\varphi = (\varphi_1 + \varphi_2)/2$ and $\phi = \pi\Phi/\Phi_0$ ($\Phi_0 \simeq 2 \times 10^{-15}$ Wb is the flux quantum) is the normalized magnetic flux. If $I_{c,i}$ ($i = 1, 2$) is the critical current of the i th junction, we have

$$\begin{aligned} I_+ &= I_{c,1}(T_e) + I_{c,2}(T_{\text{bath}}), \\ r &= \frac{I_{c,1}(T_e) - I_{c,2}(T_{\text{bath}})}{I_{c,1}(T_e) + I_{c,2}(T_{\text{bath}})}. \end{aligned} \quad (4)$$

To write Eq. (3) in this way, it is important to assume that the Josephson weak links have the same resistance R_N but different critical currents, i.e., $I_{c,1} \neq I_{c,2}$. The choice of keeping R_N fixed is arbitrary, since the only physical important parameter is the asymmetry of the junction critical currents needed to increase the photon absorption effect. The main advantage is that it allows us to simplify the analytic and numerical treatment. Similar results can be obtained if we assume different junction resistances. Experimentally, to have the same resistance, the junction should be fabricated in a particular way. A different length in the weak links determines a difference in the Thouless energy (which scales as l^2). This difference in length must be balanced by different cross-sectional areas, since we want equal resistance in the junctions.

Under these hypotheses, the dynamics of the phase and the applied voltage V are given by the resistively and capacitively shunted Josephson junction (RCSJ) model [19,24]. We model the SQUID as a capacitor C , a resistor R , and a nonlinear magnetic flux-dependent inductance L_J , arranged in a parallel configuration. The equation for φ can be written in terms of the dimensionless variable $\tau = 2\pi v t$, as [24]

$$c \frac{d^2\varphi}{d\tau^2} + \frac{d\varphi}{d\tau} + \alpha[f(\varphi, \tau) - \delta] = 0, \quad (5)$$

where $\delta = I_B/I_+$, $c = 2\pi RCv$, $f(\varphi, \tau) = I_J[\varphi; \phi(\tau)]/I_+$, and $\alpha = I_+R/(\Phi_0v)$. In the following, we consider the case in which the junction capacitances are negligible and there is no bias current flowing through the SQUID, i.e., $c = 0$ and $\delta = 0$.

Before solving Eq. (5) numerically, it is useful to have a qualitative understanding of the effect induced by photon

absorption. This can be done by analyzing the behavior of the Josephson energy as a function of the magnetic flux Φ and the time-dependent critical current $I_{c,1}$. The Josephson energy reads [19,24]

$$\begin{aligned} E_J &= \alpha \int d\varphi I_J = -\alpha \left[I_{c,1} \cos \left(\varphi + \frac{\pi\Phi}{\Phi_0} \right) \right. \\ &\quad \left. + I_{c,2} \cos \left(\varphi - \frac{\pi\Phi}{\Phi_0} \right) \right]. \end{aligned} \quad (6)$$

Let us set consider the case in which the external magnetic flux is $\Phi/\Phi_0 = 1/2 - \chi/\pi$ with $\chi \ll 1$, i.e., close to an instability point [19].

For the sake of discussion, let us discuss first the case in which $I_{c,1}(t = 0) \gg I_{c,2}$. In this case, the Josephson energy reads $E_J/E_{J,0} \approx -\cos[\varphi + \pi(\Phi/\Phi_0)] = -\sin(\varphi - \chi)$, which has a minimum at $\varphi = (4m + 1)\pi/2 - \chi$ (with m integer).

When the photon is absorbed, $I_{c,1}$ decreases exponentially and becomes much smaller than $I_{c,2}$. The Josephson energy reads $E_J/E_{J,0} \approx -\cos[\varphi - \pi(\Phi/\Phi_0)] = -\cos(\varphi + \chi - \pi/2) = -\sin(\varphi + \chi)$, which has a minimum at $\varphi = (4k + 1)\pi/2 + \chi$ (with k integer). The two energy minima are shifted by $\Delta\varphi = 2\pi(m - k) - 2\chi$ and the closest *nontrivial* jump, i.e., $m \neq k$, is obtained for $\Delta\varphi \approx 2\pi$.

In the realistic implementation, we have $I_{c,1}(t = 0) \approx I_{c,2}$ [see Fig. 2(a), where $r(t = 0) \approx 0$]. This is represented in Fig. 1(b), where we pictorially show how the change in the Josephson potential energy can induce the phase jump. It is important to notice that this energetic discussion does not provide information about the amplitude of the jump (which can be $|\Delta\varphi| = 2\chi, 2\pi - 2\chi, 4\pi - 2\chi, \dots$). This must be determined by solving the full dynamics of the junction temperature [Eq. (2)] and phase dynamics [Eq. (5)]. An example of the dynamical behavior of T_e , $I_{c,1}$, r , φ , and $V(t)$ is shown in Figs. 2(a) and 2(b).

Note that while in the original paper [19] the phase undergoes a π jump, here the jump is of 2π . This difference is related to the nature of perturbation of the Josephson energy landscape. While in Ref. [19] the time-dependent magnetic field induces the Josephson energy modulation, here it is the asymmetry of two junctions induced by the photon absorption.

IV. THE VOLTAGE DEPENDENCE ON THE JUNCTION AND DRIVE PARAMETERS

The voltage generated across the SQUID vs time is shown in Fig. 3 as a function of various parameters: the photon frequency v in Fig. 3(a), the bath temperature T_{bath} in Fig. 3(b), the asymmetry parameter ϵ in Fig. 3(c), and the applied magnetic flux Φ in Fig. 3(d).

Figure 3(a) shows that for a photon frequency above 5 THz, the SQUID generates a sizable voltage pulse at

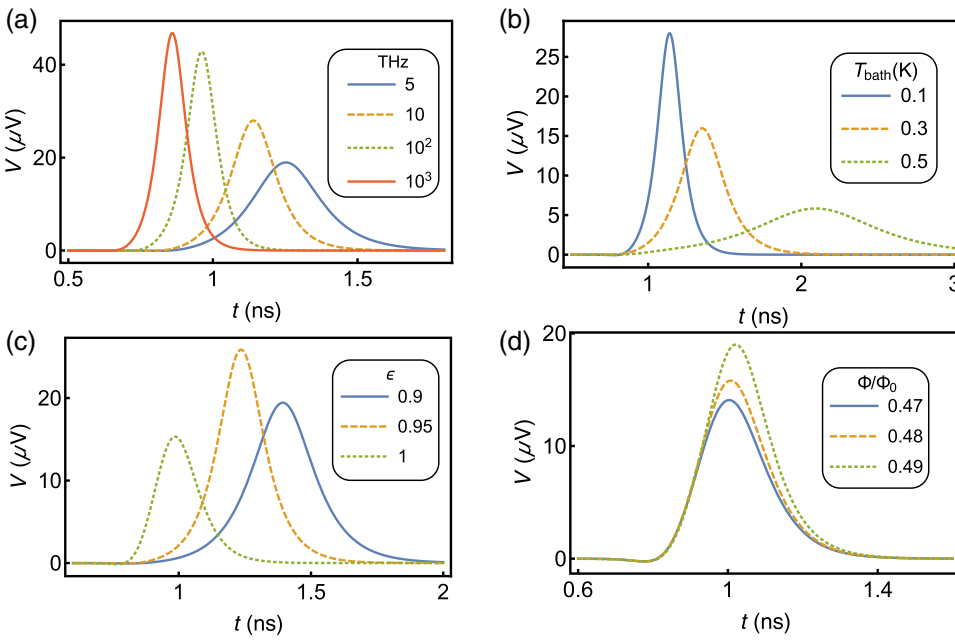


FIG. 3. (a) The voltage-pulse dynamics for different absorbed photon frequencies ν at $T_{\text{bath}} = 100$ mK, $\Phi/\Phi_0 = 0.499$, and $\epsilon = 0.98$. (b) The voltage-pulse dynamics for different bath temperatures T_{bath} at $\nu = 10$ THz, $\Phi/\Phi_0 = 0.499$, and $\epsilon = 0.98$. (c) The voltage-pulse dynamics for different asymmetry parameters ϵ at $T_{\text{bath}} = 100$ mK, $\nu = 10$ THz, and $\Phi/\Phi_0 = 0.499$. (d) The voltage-pulse dynamics for different magnetic fluxes Φ at $T_{\text{bath}} = 100$ mK, $\nu = 10$ THz, and $\epsilon = 0.98$.

$T_{\text{bath}} = 0.1$ K. The voltage-pulse maximum increases with the photon frequency, ranging from $20 \mu\text{V}$ at $\nu = 5$ THz to $40 \mu\text{V}$ at $\nu = 100$ THz.

Another relevant parameter is the working temperature T_{bath} [shown in Fig. 3(b) for $\nu = 10$ THz]. At low temperature ($T_{\text{bath}} = 0.1$ K), the temperature jump in the junction is large and leads to an increased asymmetry and to large voltage pulses (solid blue curve). At a higher temperature ($T_{\text{bath}} = 0.5$ K), the voltage pulse is broadened, with a smaller maximum around $5 \mu\text{V}$, which means that the device can work even at these temperatures.

The PSRD works at best for a small asymmetry parameter ϵ , as shown in Fig. 3(c). This is because the asymmetry induced by the photon absorption is maximized. A possible asymmetry range is $0.9 \leq \epsilon \leq 1$.

The magnetic flux Φ must be close to a critical point in order to locate the SQUID at an unstable point, i.e., $\Phi/\Phi_0 = 0.5$. The best performance is obtained for $\Phi/\Phi_0 = 0.499$, but the voltage pulse is also sizable for $\Phi/\Phi_0 = 0.47$. However, in deciding the optimal applied magnetic flux, we must also consider the effect of noise (see Sec. VI below). As a matter of fact, if the system is too close to an instability point, the noise could induce an undesired transition.

V. PHOTON DETECTION

A. Detection of arrival of photon

The PSRD can be efficiently used to detect an arriving photon. We can think of connecting the device to a discriminator circuit that is triggered as soon as the voltage generated by the PSRD exceeds a detection threshold V_{\min} . Figure 4(a) shows the maximum voltage V_{\max} reached as a function of the photon frequency for bath temperatures

$T_{\text{bath}} = 0.1, 0.3$, and 0.5 K. If, for instance, we set a detection threshold of $V_{\min} = 5 \mu\text{V}$ (red dashed line in Fig. 4), photons with frequency ν above 10 THz can be detected even at a bath temperature of $T_{\text{bath}} = 0.5$ K.

Figure 4(b) shows the maximum voltage V_{\max} as a function of bath temperature and for various photon frequencies. For $V_{\min} = 5 \mu\text{V}$, while photons of 1 THz are at the limit of measurability, for a higher frequency, i.e., $\nu \geq 10$ THz, the PSRD is able to detect their arrivals even at high temperature.

B. Detection of photon frequency

With the PSRD, it is also possible to determine the frequency of the detected photon, i.e., one can use it as a calorimeter. In order to have a sizable voltage output, we focus on photons with $\nu \geq 1$ THz. To see if it is possible to distinguish the frequency of the absorbed photon, we need to analyze the signal-to-noise (S/N) ratio and the resolving power. The first of these can be defined as [34]

$$\frac{S}{N}(h\nu) = \frac{V(\nu = 0, T_{\text{bath}}) - V(h\nu, T_{\text{bath}})}{\sqrt{\mathcal{S}_V(T_{\text{bath}})\omega}}, \quad (7)$$

where $V(\nu = 0, T_{\text{bath}})$ and $V(h\nu, T_{\text{bath}})$ are the voltages generated when no-photon is absorbed and a photon of frequency ν is absorbed, respectively. The function $\mathcal{S}_V(T_{\text{bath}})$ and ω are the voltage noise spectral density and the detector bandwidth, respectively. The noise spectral density is determined by the Johnson noise spectral density $\mathcal{S}_V(T_{\text{bath}}) = 4k_B T_{\text{bath}} R_N$ in the absence of radiation. The bandwidth must satisfy the relation $\omega \geq 2\pi/\tau_{e-\text{ph}}$ [34]. Since we are working at moderately low temperature, i.e., $T_{\text{bath}} = 0.1$ K, we can assume [25] that $\tau_{e-\text{ph}} \approx 10^{-4}$ s.

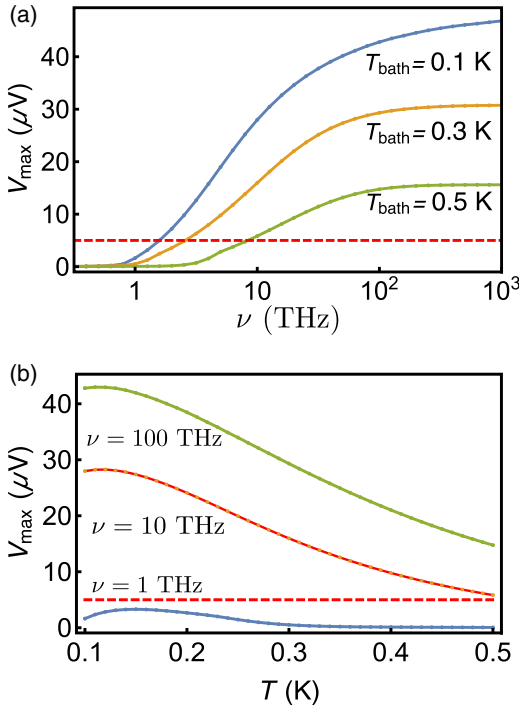


FIG. 4. (a) The maximum voltage V_{\max} generated at the extremes of the SQUID as a function of the frequency of the absorbed photon at different bath temperatures. (b) V_{\max} as a function of the working bath temperature for different energies of the incoming photons. The red dashed lines indicate a voltage threshold detection of $5 \mu\text{V}$.

Moreover, the voltage pulse has a typical width of a fraction of a nanosecond (see Fig. 2), so that to be able to detect it, we need sufficiently high-frequency resolution. In the following, we consider a detector bandwidth of $\omega = 10 \text{ GHz}$, which should allow us to detect the main features of a large range of voltage pulses.

With the above assumption, we obtain, for the S/N ratio,

$$\left| \frac{S}{N}(h\nu) \right| = \frac{V_{\max}(h\nu, T_{\text{bath}})}{\sqrt{4k_B T_{\text{bath}} R_N \omega}}, \quad (8)$$

where $V_{\max}(h\nu, T_{\text{bath}})$ is the maximum voltage generated by the photon, and is extracted from Fig. 4(a). The behavior of the S/N ratio for $\omega = 10 \text{ GHz}$ is shown in Fig. 5(a) and, as expected, closely resembles the shape of the maximum achievable voltage displayed in Fig. 4(a). We note that, for a photon with $\nu \geq 10 \text{ THz}$, we obtain a large $S/N \geq 5$ even at a high working temperature $T_{\text{bath}} = 0.5 \text{ K}$. In the lower-frequency range, the radiation-sensing limitation is given by the voltage signal strength, as discussed in the previous section.

The other figure of merit that characterizes the performance of the PSRD is the resolving power, defined as

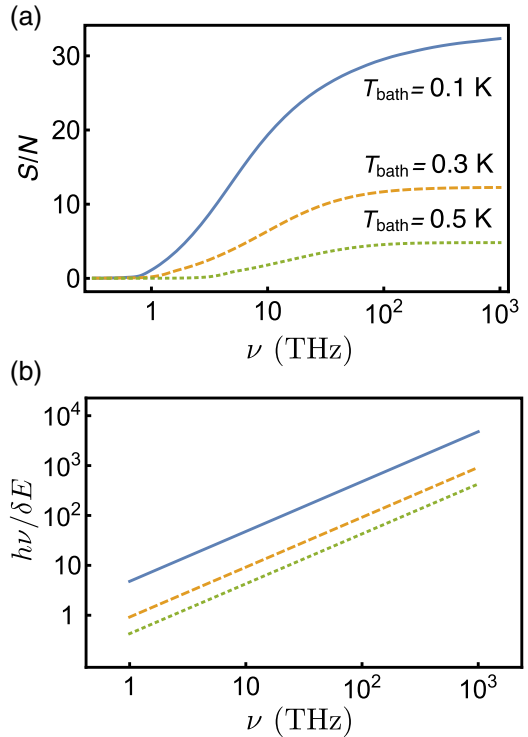


FIG. 5. (a) The PSRD signal-to-noise (S/N) ratio as a function of the frequency of the absorbed photon and for various bath temperatures. The detection bandwidth is set to $\omega = 10 \text{ GHz}$. (b) The resolving power $h\nu/\delta E$ as a function of the frequency of the absorbed photon and for various bath temperatures. The temperatures are $T_{\text{bath}} = 0.1, 0.3, 0.5 \text{ K}$ (solid blue, dashed orange, and dotted green line, respectively) as in (a).

follows [34]:

$$\frac{h\nu}{\delta E} = \frac{h\nu}{4\sqrt{2 \log 2k_B T_{\text{bath}}^2 C_e}}. \quad (9)$$

As shown in Fig. 5(b), $h\nu/\delta E$ increases linearly with the photon frequency and for $\nu \geq 10 \text{ THz}$ it exceeds 10 at $T_{\text{bath}} = 0.1 \text{ K}$.

VI. THE THERMAL NOISE EFFECT

To achieve good detecting performance, the PSRD must be set in an unstable state (determined by the externally applied magnetic flux). The arrival of a photon induces a perturbation and thereby the phase dynamics and the voltage generation across the SQUID. In principle, any perturbation can induce the phase dynamics. For this reason, it is of crucial importance to analyze the impact of external noise sources.

In the following, we consider the effect of the thermal environment, which is expected to be the predominant source of noise. The dynamics of the PSRD are determined by a modified RCSJ equation that includes a thermal-noise

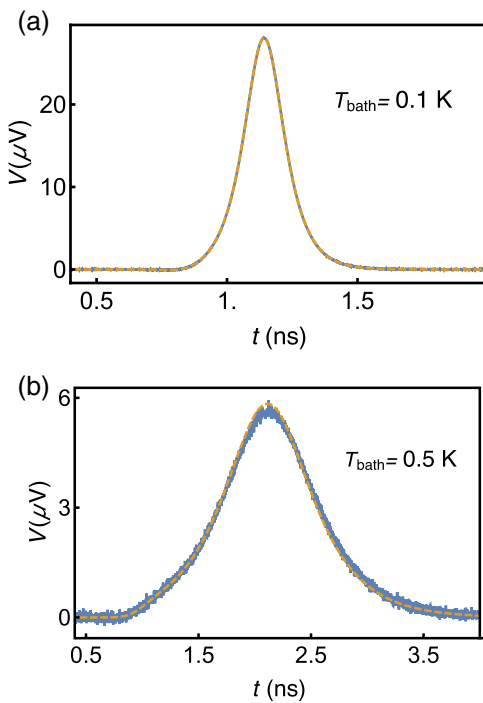


FIG. 6. A comparison between the noisy (blue curve) and noiseless voltage dynamics (dashed yellow curve) for various bath temperatures: (a) $T_{\text{bath}} = 0.1$ K; (b) $T_{\text{bath}} = 0.5$ K. The dynamics are obtained by averaging over 500 noise-dynamical realizations. For $T_{\text{bath}} = 0.1$ K, the effect of the noise is barely visible. The other chosen parameters are $\epsilon = 0.98$, and $\Phi/\Phi_0 = 0.499$.

contribution. This can be written in terms of a Langevin RCSJ equation [19]:

$$\frac{\hbar}{2eR}\dot{\varphi} + \alpha[f(\varphi, \tau) - \delta] = \xi(t), \quad (10)$$

where $\xi(t)$ is the white-noise contribution, with correlation function

$$\langle \xi(t)\xi(t') \rangle = \frac{2k_B T_{\text{bath}}}{R_N} \delta(t - t'). \quad (11)$$

The voltage dynamics in the presence of noise averaged over 500 noise realizations are shown in Fig. 6. As can be seen, the effect of noise is barely visible up to high temperatures with $T_{\text{bath}} = 0.5$ K. Furthermore, even in this situation, the main dynamical features, such as the shape and the maximum amplitude of the voltage pulse, are fully preserved. From this, it follows that the performance of the PSRD is almost unmodified by the presence of thermal noise.

VII. CONCLUSIONS

In summary, we propose a design for a single-photon sensor based on the proximity effect, and on the instability

induced by the absorption of a photon. In a SQUID configuration, two proximity SNS junctions can be set in an unstable state by controlling an applied magnetic flux piercing the superconducting loop. The absorbed photon induces an enhancement of the electronic temperature in the absorbing junction and, as a final result, a voltage spike across the interferometer. With our choice of realistic parameters for the structure, this signal is strong enough to be measured using conventional electronics. The voltage-pulse shape and its amplitude depend on the photon frequency, the junction asymmetry, and the working bath temperature, and could be measured in several different configurations as soon as the photon frequency is greater than ~ 1 THz. A straightforward use of the PSRD is as a photon-arrival detector. In addition, it can also work as a calorimeter, since it is able to distinguish an absorbed photon frequency in the range $1 \text{ THz} \leq \nu \leq 10^3 \text{ THz}$. The achievable signal-to-noise ratio and resolving power suggest high performance when the PSRD works at moderately low temperatures around 0.1 K. Furthermore, the performance of the detector is basically unaffected by the working temperature (between 0.1 and 0.5 K) and the presence of thermal noise. These features make the PSRD interesting for a number of different applications; for instance, we can envision its use in quantum technologies as well as in astrophysics.

ACKNOWLEDGMENTS

PS has received funding from the European Union (Grant No. FP7/2007–2013) under REA Grant Agreement No. 630925—COHEAT and from MIUR-FIRB2013—Project Coca (Grant No. RBFR1379UX). FG has received funding from the European Research Council under the European Union’s Seventh Framework Programme (Grant No. FP7/2007–2013) and ERC Grant Agreement No. 615187-COMANCHE, and the Tuscany Region under the FARFAS 2014 project SCIAZERO. GPP and PS have received funding from the Progetto Premiale Q-SecGroundSpace—Intermodal Secure Quantum Communication on Ground and Space D.M. n.543 del 05/08/2015.

-
- [1] B. Moision and W. Farr, Communication limits due to photon detector jitter, *IEEE Photonics Tech. L.* **20**, 715 (2008).
 - [2] N. Gisin, G. Ribordy, W. Tittel, and H. Zbinden, Quantum cryptography, *Rev. Mod. Phys.* **74**, 145 (2002).
 - [3] G. N. Gol’tsman, O. Okunev, G. Chulkova, A. Lipatov, A. Semenov, K. Smirnov, B. Voronov, A. Dzardanov, C. Williams, and R. Sobolewski, Picosecond superconducting single-photon optical detector, *Appl. Phys. Lett.* **79**, 705 (2001).
 - [4] C. M. Natarajan, M. G. Tanner, and R. H. Hadfield, Superconducting nanowire single-photon detectors: Physics

- and applications, *Supercond. Sci. Technol.* **25**, 063001 (2012).
- [5] S. Miki, M. Fujiwara, M. Sasaki, B. Baek, A. J. Miller, R. H. Hadfield, S. W. Nam, and Z. Wang, Large sensitive-area NbN nanowire superconducting single-photon detectors fabricated on single-crystal MgO substrates, *Appl. Phys. Lett.* **92**, 061116 (2008).
- [6] K. M. Rosfjord, J. K. W. Yang, E. A. Dauler, A. J. Kerman, V. Anant, B. M. Voronov, G. N. Gol'tsman, and K. K. Berggren, Nanowire single-photon detector with an integrated optical cavity and anti-reflection coating, *Opt. Express* **14**, 527 (2006).
- [7] S. Miki, T. Yamashita, M. Fujiwara, M. Sasaki, and Z. Wang, Multichannel SNSPD system with high detection efficiency at telecommunication wavelength, *Opt. Lett.* **35**, 2133 (2010).
- [8] F. Marsili, F. Najafi, E. Dauler, F. Bellei, X. Hu, M. Csete, R. J. Molnar, and K. K. Berggren, Single-photon detectors based on ultranarrow superconducting nanowires, *Nano Lett.* **11**, 2048 (2011).
- [9] S. Miki, M. Takeda, M. Fujiwara, M. Sasaki, A. Otomo, and Z. Wang, Superconducting NbTiN nanowire single photon detectors with low kinetic inductance, *Appl. Phys. Express* **2**, 075002 (2009).
- [10] H. Shibata, H. Takesue, T. Honjo, T. Akazaki, and Y. Tokura, Single-photon detection using magnesium diboride superconducting nanowires, *Appl. Phys. Lett.* **97**, 212504 (2010).
- [11] N. Curtz, E. Koller, H. Zbinden, M. Decroux, L. Antognazza, Ø. Fischer, and N. Gisin, Patterning of ultrathin YBCO nanowires using a new focused-ion-beam process, *Supercond. Sci. Technol.* **23**, 045015 (2010).
- [12] E. A. Dauler, B. S. Robinson, A. J. Kerman, J. K. W. Yang, K. M. Rosfjord, V. Anant, B. Voronov, G. Gol'tsman, and K. K. Berggren, Multi-element superconducting nanowire single-photon detector, *IEEE Trans. Appl. Supercond.* **17**, 279 (2007).
- [13] E. A. Dauler, A. J. Kerman, B. S. Robinson, J. K. Yang, B. Voronov, G. Goltsman, S. A. Hamilton, and K. K. Berggren, Photon-number-resolution with sub-30-ps timing using multi-element superconducting nanowire single photon detectors, *J. Mod. Opt.* **56**, 364 (2009).
- [14] P. M. Echternach, B. J. Pepper, T. Reck, and C. M. Bradford, Single photon detection of 1.5 THz radiation with the quantum capacitance detector, *Nat. Astron.* **2**, 90 (2017).
- [15] S. Komiyama, O. Astafiev, V. Antonov, T. Kutsuwa, and H. Hirai, A single-photon detector in the far-infrared range, *Nature* **403**, 405 EP (2000).
- [16] J. Wei, D. Olaya, B. S. Karasik, S. V. Pereverzev, A. V. Sergeev, and M. E. Gershenson, Ultrasensitive hot-electron nanobolometers for terahertz astrophysics, *Nat. Nanotechnol.* **3**, 496 EP (2008).
- [17] M. Tarkhov, D. Morozov, P. Mauskopf, V. Seleznev, A. Korneev, N. Kaurova, I. Rubtsova, O. Minaeva, B. Voronov, and G. Gol'tsman, in *Proc. 17th Int. Symp. Space Terahertz Technology, Paris*, 120 (Curran Associates, Inc., Red Hook, NY, 2006).
- [18] F. Giazotto, M. Martínez-Pérez, and P. Solinas, Coherent diffraction of thermal currents in Josephson tunnel junctions, *Phys. Rev. B* **88**, 094506 (2013).
- [19] P. Solinas, S. Gasparinetti, D. Golubev, and F. Giazotto, A Josephson radiation comb generator, *Sci. Rep.* **5**, 12260 EP (2015).
- [20] F. Giazotto and M. J. Martínez-Pérez, The Josephson heat interferometer, *Nature* **492**, 401 (2012).
- [21] P. Solinas, R. Bosisio, and F. Giazotto, Radiation comb generation with extended Josephson junctions, *J. Appl. Phys.* **118**, 113901 (2015).
- [22] R. Bosisio, F. Giazotto, and P. Solinas, Parasitic effects in superconducting quantum interference device-based radiation comb generators, *J. Appl. Phys.* **118**, 213904 (2015).
- [23] T. Udem, R. Holzwarth, and T. W. Hänsch, Optical frequency metrology, *Nature* **416**, 233 (2002).
- [24] M. Tinkham, *Introduction to Superconductivity* (McGraw-Hill, New York, 1996).
- [25] F. Giazotto, T. T. Heikkilä, G. P. Pepe, P. Helistö, A. Luukanen, and J. P. Pekola, Ultrasensitive proximity Josephson sensor with kinetic inductance readout, *Appl. Phys. Lett.* **92**, 162507 (2008).
- [26] J. Voutilainen, M. A. Laakso, and T. T. Heikkilä, Physics of proximity Josephson sensor, *J. Appl. Phys.* **107**, 064508 (2010).
- [27] A. D. Zaikin and G. F. Zharkov, Effect of external fields and impurities on the Josephson current in SNINS junctions, *Sov. J. Low Temp. Phys.* **7**, 184 (1981).
- [28] F. K. Wilhelm, A. D. Zaikin, and G. Schön, Supercurrent in a mesoscopic proximity wire, *J. Low Temp. Phys.* **106**, 305 (1997).
- [29] F. Giazotto, T. T. Heikkilä, A. Luukanen, A. M. Savin, and J. P. Pekola, Opportunities for mesoscopics in thermometry and refrigeration: Physics and applications, *Rev. Mod. Phys.* **78**, 217 (2006).
- [30] F. Zhou, P. Charlat, B. Spivak, and B. Pannetier, Density of states in superconductor–normal metal–superconductor junctions, *J. Low Temp. Phys.* **110**, 841 (1998).
- [31] H. Rabani, F. Taddei, O. Bourgeois, R. Fazio, and F. Giazotto, Phase-dependent electronic specific heat of mesoscopic Josephson junctions, *Phys. Rev. B* **78**, 012503 (2008).
- [32] H. Rabani, F. Taddei, F. Giazotto, and R. Fazio, Influence of interface transmissivity and inelastic scattering on the electronic entropy and specific heat of diffusive superconductor–normal metal–superconductor Josephson junctions, *J. Appl. Phys.* **105**, 093904 (2009).
- [33] T. T. Heikkilä and F. Giazotto, Phase sensitive electron-phonon coupling in a superconducting proximity structure, *Phys. Rev. B* **79**, 094514 (2009).
- [34] P. Virtanen, A. Ronzani, and F. Giazotto, Josephson Photodetectors via Temperature-to-Phase Conversion, *Phys. Rev. Applied* **9**, 054027 (2018).
- [35] T. Heikkilä, R. Ojajärvi, I. Maasilta, F. Giazotto, and F. Bergeret, Thermoelectric radiation detector based on superconductor/ferromagnet systems. arXiv preprint arXiv:1709.08856 (2017).
- [36] C. Guarcello, P. Solinas, M. Di Ventra, and F. Giazotto, Hysteretic Superconducting Heat-Flux Quantum Modulator, *Phys. Rev. Applied* **7**, 044021 (2017).
- [37] C. Guarcello, P. Solinas, A. Braggio, M. Di Ventra, and F. Giazotto, Josephson Thermal Memory, *Phys. Rev. Applied* **9**, 014021 (2018).